Journal of Geophysical Research: Solid Earth

Supporting Information for

Along-Strike Variations of Alaska Subduction Zone Structure and Hydration Determined From Amphibious Seismic Data

Zongshan Li[1], Douglas A. Wiens[1], Weisen Shen[2], Donna J. Shillington[3]

[1]Department of Earth and Planetary Sciences, Washington University, St. Louis, MO, 63130, USA.

[2]Department of Geosciences, Stony Brook University, Stony Brook, NY, 11794, USA.

3Northern Arizona University, School of Earth and Sustainability, Flagstaff, AZ, 86001, USA.

Corresponding author: Zongshan Li (zongshan.li@wustl.edu)

Contents of this file

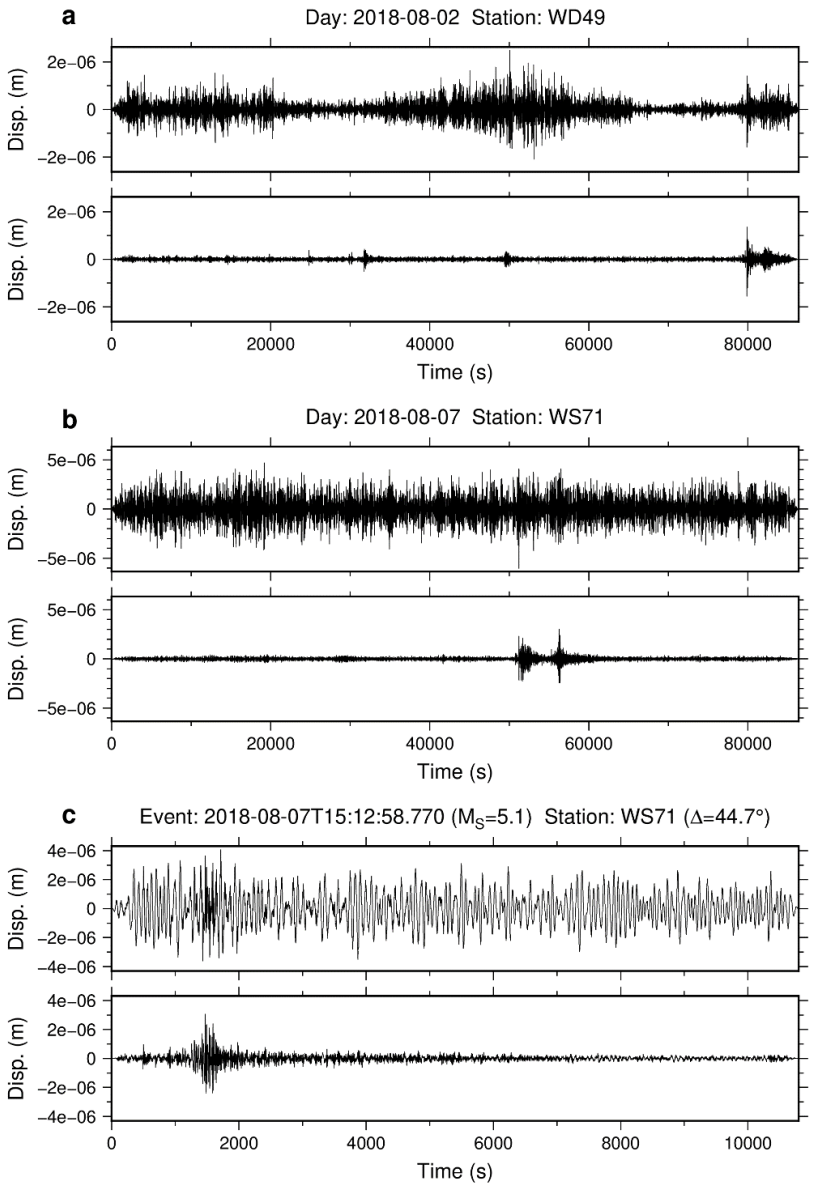

Figure S1. Examples of tilt and compliance noise removal for ocean bottom seismograph (OBS) vertical component records in displacement units. All waveforms are plotted after applying a bandpass filter between 10 and 100 s. **(a)** Daily length seismic waveform of AACSE OBS WD50 on 2018-08-02, which is dominated by tilt noises on the raw waveform (upper) but has few noises after correction (lower). **(b)** Daily length seismic waveform of AACSE OBS WS71 on 2018-08-07, an example that has strong compliance noises on the raw waveform (upper) and denoised after correction (lower). **(c)** A 10800 s length seismic waveform of the 2018-08-07T15:12:58.770 M_S = 5.1 event recorded by AACSE OBS WS71, which is a segment cut from (b). The distinct contrast before (upper) and after (lower) the noise removal suggests that noise correction is very helpful in improving surface wave signals that are obscured by the ocean bottom noises, which is especially important for smaller earthquakes recorded by OBS.

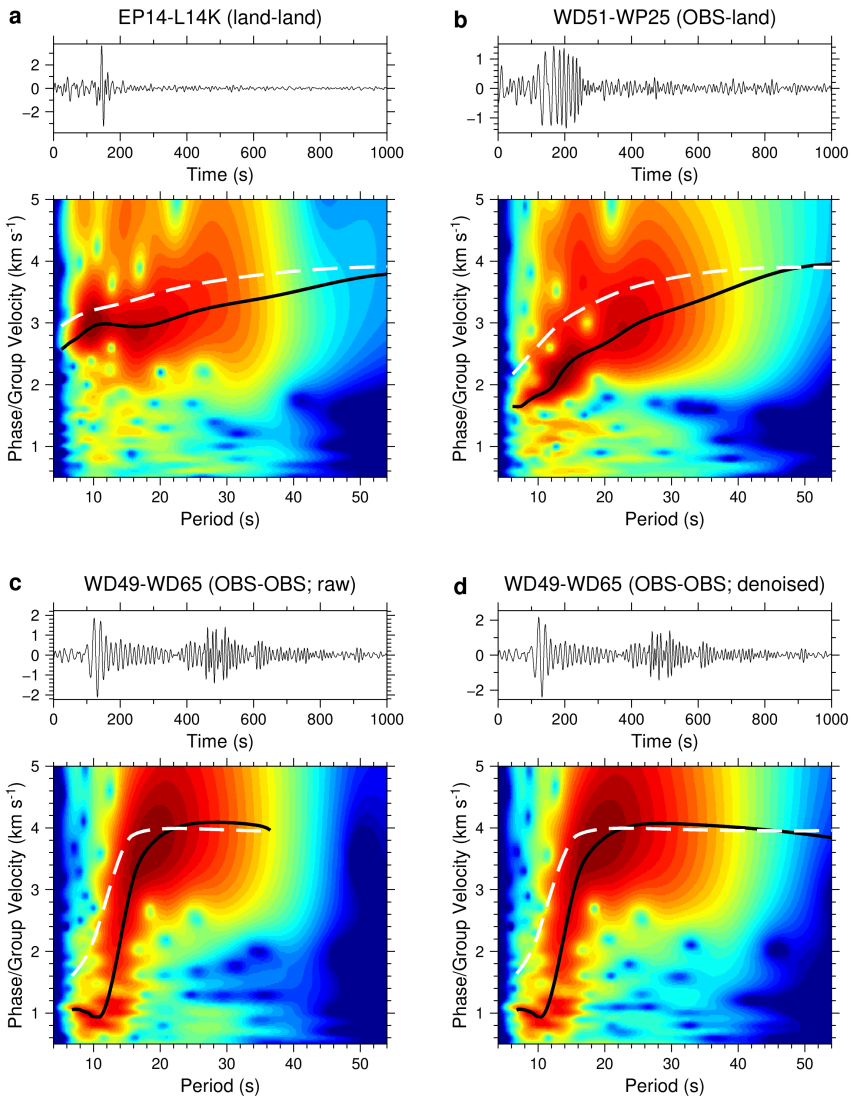

Figure S2. Examples of ambient noise cross-correlations and frequency-time analysis (FTAN) measurements for land-land pairs, OBS-land pairs, and OBS-OBS pairs, respectively. All waveforms (upper) are plotted after a bandpass filter between 8 and 36 s. All spectrums (lower) are plotted following the narrow bandpass Gaussian filtering of FTAN, with the measured group velocity dispersion curves shown as solid black lines and corresponding phase velocity dispersion curves shown as dashed white lines. **(a)** A land-land station pair between land stations EP14 and L14K, which has typical continental waveforms and dispersion curves. **(b)** An OBS-land station pair between OBS WD51 and land station WP25, which has lower velocities at shorter periods compared with the land-land pairs. **(c)** An OBS-OBS pair using raw waveforms between OBSs WD49 and WD65, which has typical oceanic dispersion curves. **(d)** An OBS-OBS pair using denoised waveforms between denoised waveforms OBS WD49 and WD65. It also shows typical oceanic dispersion curves, but with stronger signals at longer periods and achieves measurements at periods > 40 s.

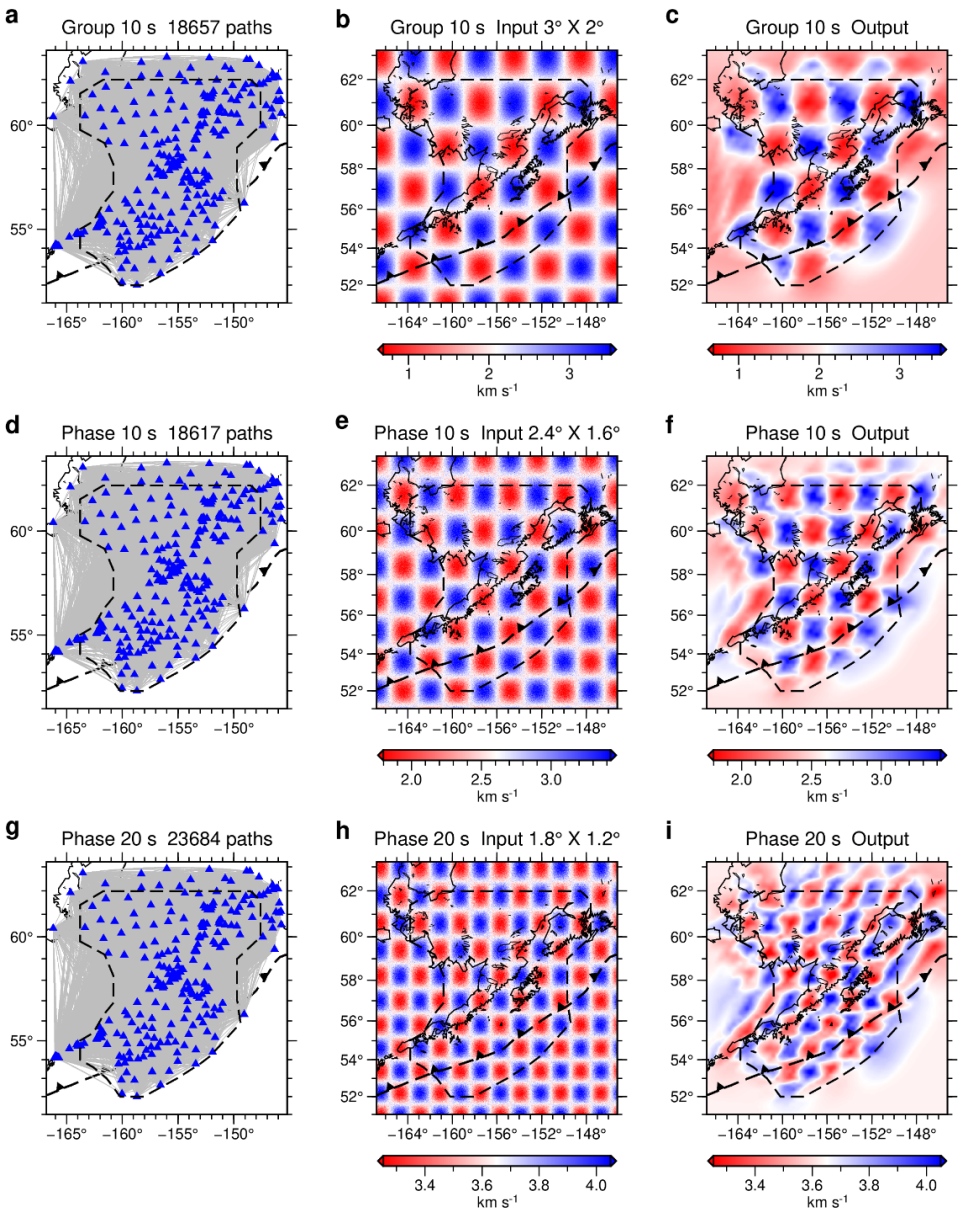

Figure S3. Checkerboard resolution tests of ambient noise tomography (ANT). Examples are shown for group and phase velocity at 10 s, and phase velocity at 20 s. The results suggest that resolution depends on the velocity range, noise perturbation, and ray path coverage. The parameters of 0.3°×0.2° grid spacing and 0.5° isotropic cells are reasonable to apply ambient noise tomography. **(a-c)** The group velocity at 10 s has 18657 paths and could recover 3°×2° checkerboards after ANT. To make the input model close to real data, we add some Gaussian noises with std = 0.10 km s^{-1} to the checker velocities. **(d-f)** The phase velocity at 10 s has 18617 paths and could recover 2.4°×1.6° checkerboard, with some Gaussian noises of std = 0.10 km s^{-1} added. **(g-l)** The phase velocity at 20 s has 23684 paths and could recover 1.8°×1.2° checkerboard, with some Gaussian noises of std = 0.05 km s^{-1} added.

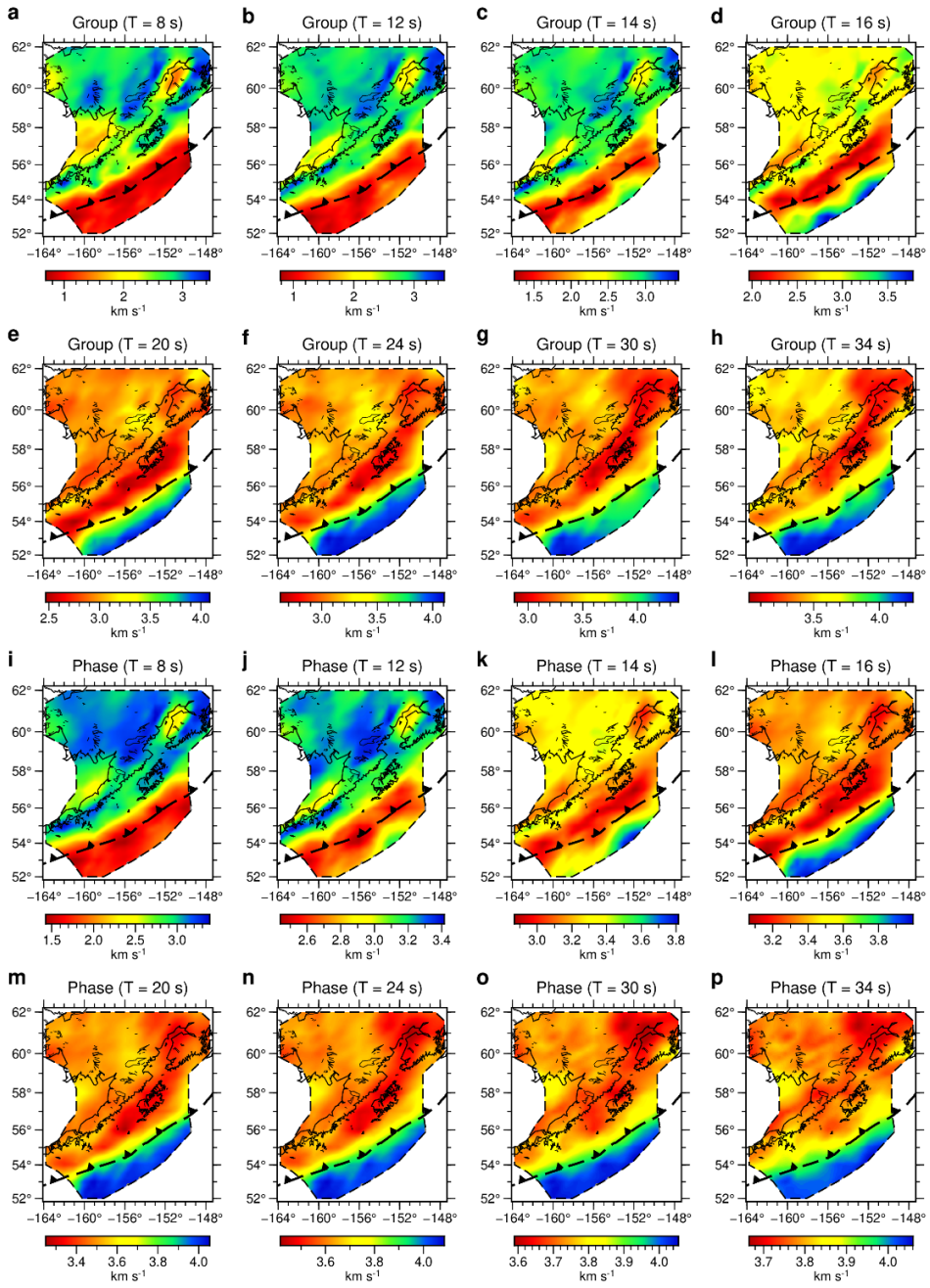

Figure S4. Rayleigh wave group and phase velocity maps from ambient noise tomography (ANT). The dashed black contour indicates our study area with reliable results. At short periods (8-14 s), the group and phase velocity maps reflect the very shallow structure and water depth, where incoming plate and trench are dominated by low-speed anomalies and mountain ranges show high-speed anomalies. At longer periods (20-30 s), the group and phase velocity maps reflect the crust and uppermost mantle structure, where the incoming plate is dominated by high-speed anomalies and low-speed anomalies cover the forearc region. **(a-h)** Group velocity maps from 8 to 34 s. **(i-p)** Phase velocity maps from 8 to 34 s.

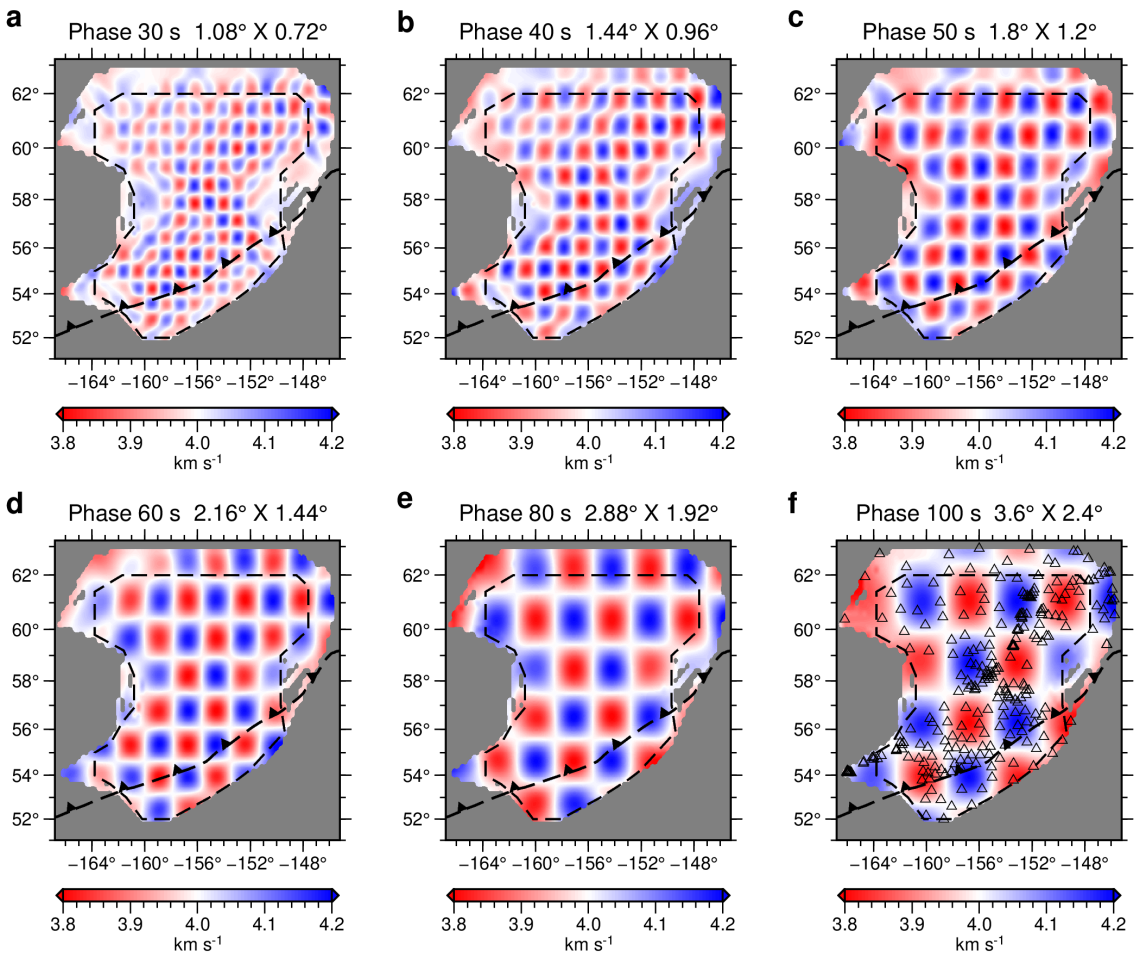

Figure S5. Checkerboard resolution tests of teleseismic Eikonal tomography (ET), which are for Rayleigh phase velocity at some example periods. The dashed black contour indicates our study area chosen to invert for 3-D V_{SV} model. **(a-f)** Phase velocity checkerboard tests at 30, 40, 50, 60, 80, 100 s, respectively. The checker size is approximately the Rayleigh wavelength, ranging from 1.08°×0.72° at 30 s to 3.6°×2.4° at 100 s. To make the input model close to real data, we add some Gaussian noises with std = 0.025 km s^{-1} to the checker velocities. The distribution of stations is marked in **(f)**. The grid spacing is 0.3°×0.2° and multichannel cross-correlations is performed for station pairs within 410 km. The results suggest that above parameters work well to recover the input anomalies.

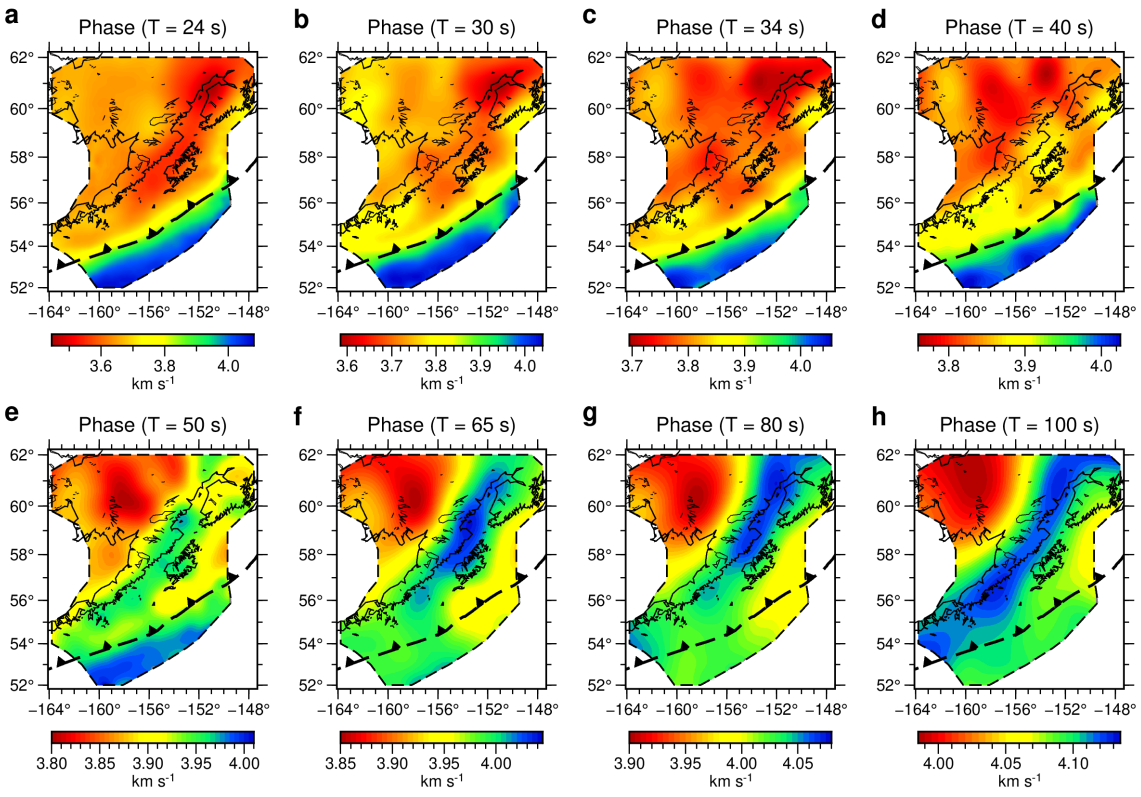

Figure S6. Rayleigh wave phase velocity maps from teleseismic Helmholtz tomography (HT) at example periods. The dashed black contour is determined by the region with reliable results. **(a-h)** Rayleigh wave phase velocity maps at 24 s to 100 s from HT. These phase velocity maps constrain the lower crust and uppermost mantle structure. At 40 s period, the high-velocity anomalies still dominate the incoming plate region and also extend north across the Aleutian Trench a little bit compared to the 24 s phase velocity map. At even longer periods (e.g., 60, 100 s), the trench region is replaced by low velocity, and high-speed anomalies gradually occupy the volcanic arc.